Implementation and Sensorless Vector-Control Design and Tuning Strategy for SMPM Machines in Fan-Type Applications

Parag Kshirsagar, *Member, IEEE*, Rolando P. Burgos, *Member, IEEE*, Jihoon Jang, *Member, IEEE*, Alessandro Lidozzi, Fei Wang, *Fellow, IEEE*, Dushan Boroyevich, *Fellow, IEEE*, and Seung-Ki Sul, *Fellow, IEEE*

***Abstract*—This paper presents a complete design methodology for the sensorless vector control of permanent-magnet synchronous machine (PMSM) motor drives in fan-type applications. The proposed strategy is built over a linear asymptotic state observer used to estimate the PMSM back EMF and a novel tracking controller based on a phase-locked loop system, which, by synchronizing the estimated and actual $d-q$ frames, estimates the rotor speed and position. This paper presents the complete derivation of all associated control loops, namely, state observer; tracking controller; $d-q$-axis current regulator; speed controller; an antisaturation control loop, which provides inherent operation in the flux-weakening region; and all corresponding antiwindup loops. Detailed design rules are provided for each of these loops, respectively verified through time-domain simulations, frequency-response analysis, and experimental results using a three-phase 7.5-kW PMSM motor drive, validating both the design methodology and the expected performance attained by the proposed control strategy.**

***Index Terms*—Luenberger observer, sensorless, SMPM, vector control.**

Manuscript received December 28, 2011; revised April 25, 2012; accepted May 14, 2012. Date of publication November 16, 2012; date of current version December 31, 2012. Paper 2011-IDC-797.R1, presented at the 2006 IEEE Industry Applications Society Annual Meeting, Tampa, FL, October 8–12, and approved for publication in the IEEE TRANSACTIONSON INDUSTRY APPLICATIONS by the Industrial Drives Committee of the IEEE Industry Applications Society. This work was supported in part by the National Science Foundation (NSF) under NSF Award EEC-9731677 and in part by the Center for Power Electronics Systems Industry Partnership Program.

P. Kshirsagar is with the United Technologies Research Center, East Hartford, CT 06108 USA, and also with Virginia Polytechnic Institute and State University, Blacksburg, VA 24061 USA (e-mail: kshirsp@utrc.utc.com).

R. P. Burgos is with ABB Corporate Research, United States Corporate Research Center, Raleigh, NC 27606-5200 USA (e-mail: rburgos@ieee.org).

J. Jang is with the General Motors Advanced Technology Center, Torrance, CA 90505 USA (e-mail: jihoon.s.jang@gmail.com).

A. Lidozzi is with Roma Tre University, 00154 Rome, Italy (e-mail: lidozzi@uniroma3.it; lidozzi@ing.uniroma3.it).

F. Wang is with The University of Tennessee, Knoxville, TN 37996 USA, and also with Oak Ridge National Laboratory, Oak Ridge, TN USA (e-mail: fred.wang@utk.edu).

D. Boroyevich is with Virginia Polytechnic Institute and State University, Blacksburg, VA 24061 USA (e-mail: dushan@vt.edu).

S.-K. Sul is with Seoul National University, Seoul 151-744, Korea (e-mail: sulsk@plaza.snu.ac.kr).

Color versions of one or more of the figures in this paper are available online at http://ieeexplore.ieee.org.

Digital Object Identifier 10.1109/TIA.2012.2227135

I. INTRODUCTION

PERMANENT-MAGNET synchronous machines (PMSMs) are controlled by using the rotor position information to synchronize the machine line currents and their sinusoidal back EMF. The rotor position may be obtained using resolvers or encoders depending on the level of accuracy required by the application. Regardless of this choice, these position transducers have inherent disadvantages, such as a reduced reliability due to their sensitivity to vibration, humidity corrosive refrigerants, high temperature, and electromagnetic noise, as well as increased costs, weight, and volume. For these reasons, the sensorless control of PMSM has become increasingly attractive.

The sensorless control for these permanent-magnet (PM) machines can be divided into two categories, one based on the back-EMF estimation and the other based on the saliency phenomena of the machine. While the former strategies reveal good performance in the high-speed region, they fail in the low-speed region and simply cannot operate at zero speed, as opposed to the latter strategies which can operate in the low-speed region including standstill. The tradeoff for using these latter strategies is a higher overall complexity and much higher digital processing needs. Nonetheless, for applications operating at higher speed (typically above 0.1 p.u. of rated speed) with centrifugal-like load torque profiles, the usage of back-EMF-based estimation strategies becomes a preferred choice [1]–[8]. Accordingly, this paper addresses the sensorless vector control of fan-type applications for climate control systems.

Numerous methods have been presented so far in order to estimate the rotor position and speed of PM machines, namely, voltage integration [2], state observer including mechanical system [3], nonlinear observer [4], extended Kalman filter [5], state observer in stationary reference frame [6], and state observer in rotor reference frame [7]. All of these but [5] use a two-stage approach, i.e., they estimate the back EMF and, from it, the rotor position and speed. The advantage of this indirect approach is the greater flexibility attained to tune the estimator and PMSM speed control system; however, until now, none of this has been truly exploited, and as a result, frequency-response-based design methodologies for sensorless vector controls are hard to find for this type of motor drive.

Accordingly, this paper presents the complete design methodology for a PMSM sensorless vector control scheme using a two-stage approach. Specifically, it employs a linear

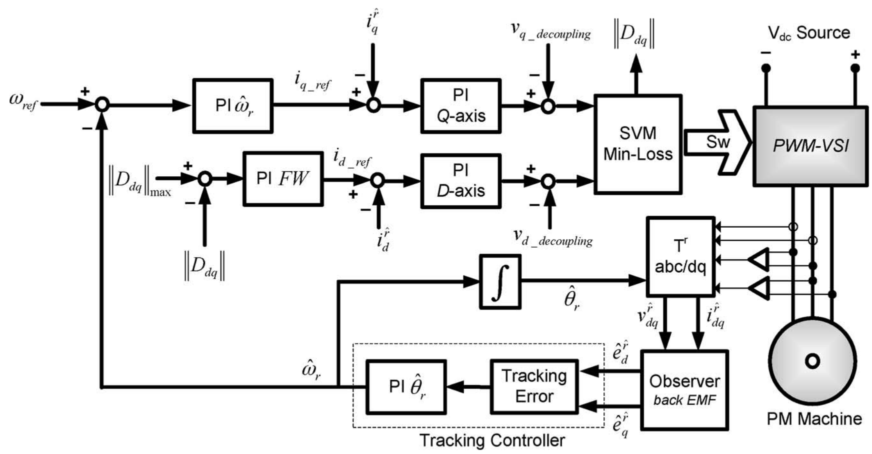

Fig. 1. Sensorless vector control scheme employed.

asymptotic state observer to estimate the machine back EMF and a tracking controller to generate the estimated speed and rotor position, the latter implemented by means of a synchronous $d{-}q$ frame phase-locked loop (PLL) system. Vector control is implemented over the estimation engine using a decoupled $d{-}q$ frame current regulator and an optimized speed-loop response covering both constant-torque and constant-power regions, where an antisaturation controller provides transparent access into the flux-weakening region of the PM machine. A detailed design procedure is provided for the proposed sensorless control strategy and verified using simulations and experimental results obtained with a 7.5-kW PMSM pulsewidth modulation (PWM) motor drive controlled using a DSP digital control system.

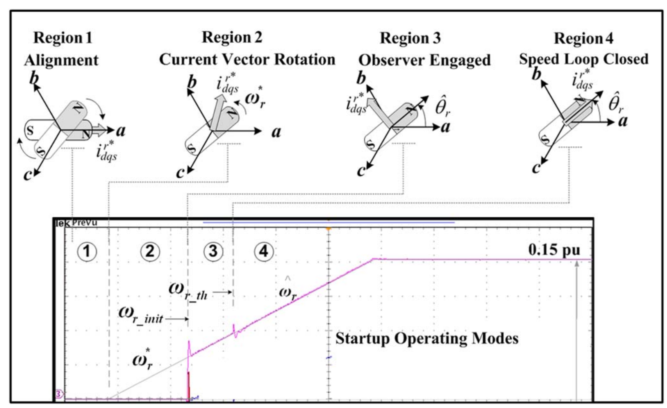

Fig. 2. Experimental result: Starting sequence employed for the proposed sensorless control strategy.

II. Sensorless Vector Control Strategy

The proposed strategy employs a linear asymptotic observer to estimate the back-EMF voltages in the rotor $d{-}q$ reference frame. These estimated quantities determine, with their relative magnitudes, the rotor position error of the machine, i.e., the angular difference between the actual and estimated $d{-}q$ frames. This error information may be readily employed under a closed-loop scheme by feeding it to the tracking controller whose output corresponds to the estimated speed of the machine, thus accelerating or decelerating the estimated $d{-}q$ frame speed in order to synchronize it with the actual frame. This estimated speed is then used to close the motor-drive speed loop and its integral—corresponding to the rotor position—used in all transformations between the abc and $d{-}q$ frames. This control structure is shown in Fig. 1, also depicting the $d{-}q$-axis current regulator and flux-weakening controller.

III. Starting Procedure

A startup procedure is mandatory for the proposed sensorless control strategy due to its dependence on the back-EMF estimation [1]. The speed range spanning from standstill to nominal speed has been divided into four operating regions as shown in Fig. 2. *Region 1* is used to align the machine; *Region 2* accelerates the machine in speed open loop while current loop is closed; in *Region 3*, the state observer and tracking controller are engaged after passing a predefined rotor velocity value ω_{r_init}; and in *Region 4*, the speed loop is closed around the threshold velocity ω_{r_th} after the estimated speed and rotor position values have converged, finally engaging the sensorless vector control algorithm. The value of the initial speed ω_{r_init}, for engaging the observer, is given as follows:

$$\omega_{r\_\mathrm{init}}\lambda_m \geq \frac{T_{\mathrm{deadtime}}}{T_{\mathrm{switching}}}V_{\mathrm{dc}} \tag{1}$$

where λ_m is the peak flux linkage of a phase, T_{deadtime} is the inverter dead-time delay, $T_{\mathrm{switching}}$ is the inverse of the switching frequency of the inverter, and V_{dc} is the inverter dc-link voltage.

At very low speed of operation (less than 0.1 p.u.) and under no load condition, the stator resistive drop and the inductive voltage drop in the motor being very small can be ignored. Then, the back-EMF voltage equals the average of the inverter output voltage, and the corresponding relation is given in (1). While (1) should be taken as a preliminary guideline, it is imperative to evaluate the lower limit for initial speed ω_{r_init} for individual cases and starting conditions in specific applications. In order to determine the threshold speed ω_{r_th}, the convergence time of the rotor position and speed estimation algorithm should be considered. Alternatively, the difference

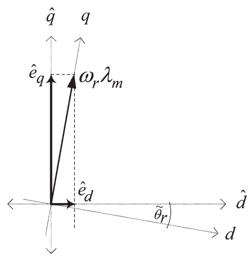

Fig. 3. Relationship between the actual and the estimated synchronous reference frames, depicting angular misalignment $\widetilde{\theta}_r$.

between the frequency of current vector and the estimated rotor speed can be used. The initial and threshold speeds chosen in this work are 0.05 and 0.08 p.u. of the rated speed, respectively.

IV. State Equations in Estimated Reference Frame

The voltage equations for SMPM machines in the actual rotor reference frame can be expressed as

$$\begin{bmatrix} v_{ds}^r \\ v_{qs}^r \end{bmatrix} = \begin{bmatrix} R_s & -\omega_r L_s \\ \omega_r L_s & R_s \end{bmatrix} \begin{bmatrix} i_{ds}^r \\ i_{qs}^r \end{bmatrix} + L_s \frac{d}{dt} \begin{bmatrix} i_{ds}^r \\ i_{qs}^r \end{bmatrix} + \omega_r \lambda_m \begin{bmatrix} 0 \\ 1 \end{bmatrix} \tag{2}$$

where v_{qs}^r and v_{ds}^r are the applied stator phase voltages in rotor reference frame, while i_{qs}^r and i_{ds}^r are the corresponding currents in the stator, ω_r is the electrical angular velocity of the rotor, R_s the per-phase stator resistance, and L_s is the per-phase stator self-inductance.

Since the real speed is not known, an alternative model is required, where the estimated rotor speed and position surrogate the real quantities. Fig. 3 shows the relationship existent between the estimated and actual $d{-}q$ frames, where the top hat ^ stands for estimated variables. The relative angular error between both frames is defined as

$$\widetilde{\theta}_r \equiv \theta_r - \hat{\theta}_r \tag{3}$$

from which a geometrical relationship can be established, relating the estimated back EMF ($e_d^{\hat{r}}$ and $e_q^{\hat{r}}$) and the actual rotor speed ω_r as follows:

$$\hat{e}_d = \omega_r \lambda_m \sin \widetilde{\theta}_r \qquad \hat{e}_q = \omega_r \lambda_m \cos \widetilde{\theta}_r. \tag{4}$$

These relations show that, when the error between reference frames is zero, the machine back EMF on the q-axis will equal $\omega_r \lambda_m$ as can been easily observed from Fig. 3.

The PM machine voltage (2) may accordingly be rewritten in the estimated rotor reference frame as shown in the following:

$$\begin{bmatrix} v_{ds}^{\hat{r}} \\ v_{qs}^{\hat{r}} \end{bmatrix} = \begin{bmatrix} R_s & -\hat{\omega}_r L_s \\ \hat{\omega}_r L_s & R_s \end{bmatrix} \begin{bmatrix} i_{ds}^{\hat{r}} \\ i_{qs}^{\hat{r}} \end{bmatrix} + L_s \frac{d}{dt} \begin{bmatrix} i_{ds}^{\hat{r}} \\ i_{qs}^{\hat{r}} \end{bmatrix} + \begin{bmatrix} -e_d^{\hat{r}} \\ e_q^{\hat{r}} \end{bmatrix}. \tag{5}$$

The back-EMF terms $\hat{e}_d^r$ and $\hat{e}_q^r$ are, however, neither state variables nor inputs to the system; therefore, in order to construct an appropriate state-space model, these variables need to be advanced to state variable status. This is possible by making the following assumption: that the rotor speed and position remain constant during a control cycle (switching period), which is true since the sampling period is significantly smaller compared to the mechanical time constants. It follows then that

$$\dot{\hat{e}}_d = 0 \qquad \dot{\hat{e}}_q = 0. \tag{6}$$

With (6), the new augmented state-space model may be readily constructed as shown in the following:

$$\dot{\mathbf{x}} = \mathbf{A}\mathbf{x} + \mathbf{B}\mathbf{u} \qquad \mathbf{y} = \mathbf{C}\mathbf{x} \tag{7}$$

with

$$\mathbf{x} = \begin{bmatrix} i_{ds}^{\hat{r}} & i_{qs}^{\hat{r}} & e_d^{\hat{r}} & e_q^{\hat{r}} \end{bmatrix}^{\mathrm{T}}$$

$$\mathbf{u} = \begin{bmatrix} v_{ds}^{\hat{r}} & v_{qs}^{\hat{r}} \end{bmatrix}^{\mathrm{T}} \qquad \mathbf{y} = \begin{bmatrix} i_{ds}^{\hat{r}} & i_{qs}^{\hat{r}} \end{bmatrix}^{\mathrm{T}}$$

$$\mathbf{A} = \begin{bmatrix} -\frac{R_s}{L_s} & \hat{\omega}_r & \frac{1}{L_s} & 0 \\ -\hat{\omega}_r & -\frac{R_s}{L_s} & 0 & -\frac{1}{L_s} \\ 0 & 0 & 0 & 0 \\ 0 & 0 & 0 & 0 \end{bmatrix}$$

$$\mathbf{B} = \begin{bmatrix} \frac{1}{L_s} & 0 \\ 0 & \frac{1}{L_s} \\ 0 & 0 \\ 0 & 0 \end{bmatrix} \qquad \mathbf{C} = \begin{bmatrix} 1 & 0 & 0 & 0 \\ 0 & 1 & 0 & 0 \end{bmatrix}. \tag{8}$$

V. Linear Asymptotic State Observer

The proposed sensorless control strategy employs a linear asymptotic state observer per Bertram's original introduction in 1961 [9], [10], having, as main feature, the use of feedback to drive the estimation error to zero. The estimator has the following form:

$$\dot{\hat{\mathbf{x}}} = A\hat{\mathbf{x}} + \mathbf{B}\mathbf{u} + \mathbf{L}\left(\mathbf{y} - \mathbf{C}\hat{\mathbf{x}}\right) \tag{9}$$

where $\mathbf{L}$, defined as

$$\mathbf{L} = \begin{bmatrix} l_{11} & l_{21} & l_{31} & l_{41} \\ l_{12} & l_{22} & l_{32} & l_{42} \end{bmatrix}^{\mathrm{T}} \tag{10}$$

is the feedback gain matrix that determines the exponential state error dynamics described by

$$\dot{\widetilde{\mathbf{x}}} = \dot{\mathbf{x}} - \mathbf{x} = (\mathbf{A} - \mathbf{L}\mathbf{C})\widetilde{\mathbf{x}} \tag{11}$$

with $\widetilde{\mathbf{x}}(0) = \mathbf{x_0} - \hat{\mathbf{x}}_\mathbf{0}$. The eigenvalues of matrix $(\mathbf{A} - \mathbf{L}\mathbf{C})$ in (11) correspond to the natural frequencies of the observer dynamics. Therefrom, the gain values of matrix $\mathbf{L}$ may be found by equalizing terms with the following characteristic equation:

$$\det(s\mathbf{I} - \mathbf{A} + \mathbf{L}\mathbf{C}) = C_o(s) = s^4 + a_1 s^3 + a_2 s^2 + a_3 s + a_4. \tag{12}$$

Since the PM machine model is an orthogonal system built over the $d{-}q$-axes, (12) may be simplified as follows:

$$C_o(s) = \left(s^2 + 2\zeta\omega_o s + \omega_o^2\right)^2. \tag{13}$$

Then, by simple inspection of (7) and (8), the gains of matrix $\mathbf{L}$ may be readily determined. First, the decoupled $d{-}q$-axis

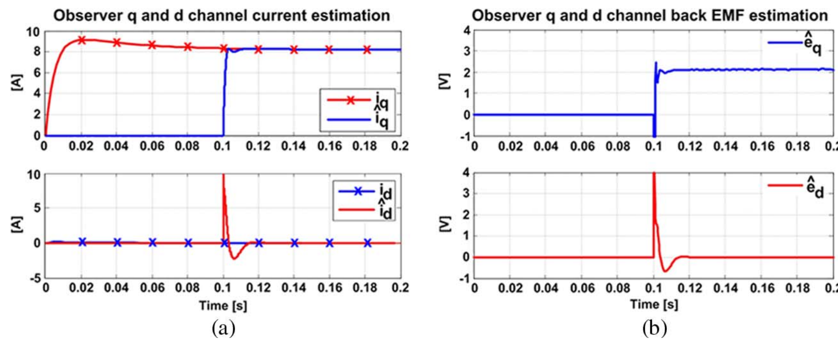

Fig. 4. Simulation results: state observer performance in rotor reference frame. (a) Current estimation. (b) Back-EMF estimation.

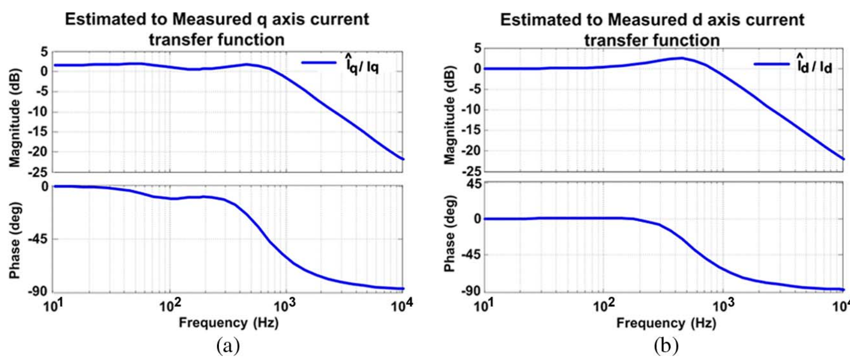

Fig. 5. Simulation results: Bode plots of estimated-to-measured currents. (a) q-axis. (b) d-axis.

dynamics implies that the estimation of the back-EMF voltages may be decoupled as well, i.e., that $\hat{e}_d^{\hat{r}}$ may be made to depend solely on $i_{ds}^{\hat{r}}$ and, correspondingly, $\hat{e}_q^{\hat{r}}$ on $i_{qs}^{\hat{r}}$. This is accomplished, indeed, if gains l_{32} and l_{41} are made equal to zero. Gains l_{11} and l_{22}, on the other hand, may be used to cancel out the electrical time constant of the machine (R_s/L_s), while gains l_{12} and l_{21} may be used to cancel out the effect of the estimated rotor speed ω_r. Matrix $\mathbf{L}$ may then be rewritten as follows:

$$\mathbf{L} = \begin{bmatrix} -\frac{R_s}{L_s} + 2\zeta\omega_o & \hat{\omega}_r \\ -\hat{\omega}_r & \frac{-R_s}{L_s} + 2\zeta\omega_o \\ \omega_o^2 L_s & 0 \\ 0 & -\omega_o^2 L_s \end{bmatrix}. \tag{14}$$

It is recommended that the bandwidth of the inner loop is at least five times the bandwidth of the outer loop [14]. Accordingly, in the proposed observer-tracking controller structure, the observer bandwidth is set to ten times the tracking controller bandwidth. Thus,

$$\omega_o = 10 \cdot \omega_t \qquad \zeta = 1/\sqrt{2} \tag{15}$$

where ω_t corresponds to the tracking controller bandwidth and ζ is the damping coefficient. The observer, as such, represents the fastest dynamic in the proposed sensorless control strategy, since the tracking controller must be faster than the speed loop. Thus, with a speed-loop bandwidth of 3 Hz, the tracking controller is set to be 20 times faster [14]; as a result, the state observer bandwidth is 600 Hz.

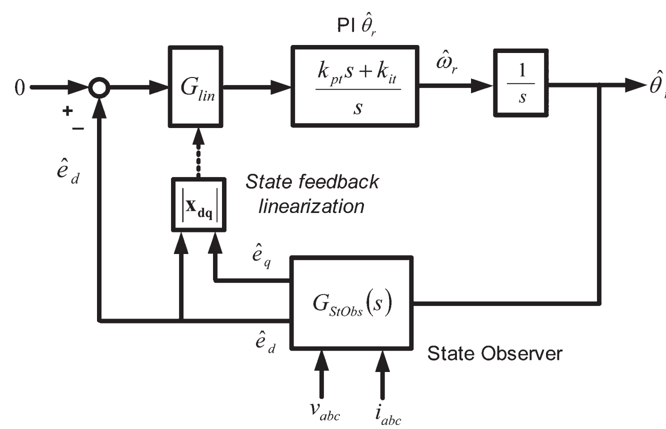

Fig. 6. PLL-based rotor speed and position estimation scheme using a PI controller to regulate the d-axis back EMF $\hat{e}_d^{\hat{r}}$ to zero.

Fig. 4 shows the dynamic response of the state observer for the PMSM motor-drive parameters given in the Appendix, showing the state variable convergence to their actual values when the enable signal goes high at time $t = 0.1$ s. Fig. 4(a) shows the $d-q$-axis currents, which clearly illustrate the convergence of the estimator since both actual and estimated variables are available, while Fig. 4(b) shows the back EMF with the d-axis component quickly converging to zero, implying alignment with the machine rotor reference frame.

The frequency response of the state observer is shown in Fig. 5, showing the actual-to-estimated transfer functions for both $d-q$-axis currents. These Bode plots show the 600-Hz resonant frequency attained by both $d-q$ channels, which was the selected bandwidth for the given design specifications.

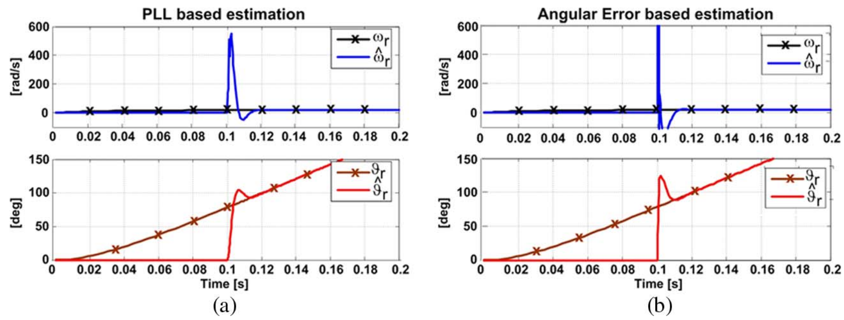

Fig. 7. Simulation results: comparison of the tracking controller schemes implemented. (a) PLL-based estimation. (b) Angular-error-based estimation.

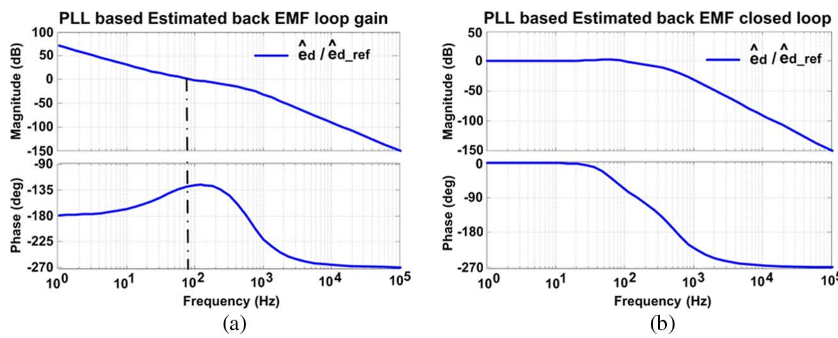

Fig. 8. Simulation results: frequency response of the PLL-based estimation technique. (a) Loop gain. (b) Closed-loop transfer function.

VI. Tracking Controller

A tracking controller estimates the speed and position of the machine based on the angular error [11]. This error is deduced from (4) as

$$\widetilde{\theta}_r = \mathrm{atan}\left(\frac{\hat{e}_d^{\hat{r}}}{\hat{e}_d^{\hat{r}}}\right). \tag{16}$$

This is a commonly used technique in sensorless control applications; however, it introduces a nonlinearity into the system and requires the usage of the inverse trigonometric function $\mathrm{atan}()$. To avoid this, an alternative tracking controller is implemented using a PLL to synchronize the estimated $d{-}q$ frame to the actual $d{-}q$ frame. This is achieved simply by regulating the d-axis back-EMF component $\hat{e}_d^{\hat{r}}$ to zero (Fig. 3). Fig. 6 shows the PLL-based tracking controller scheme, where $\hat{e}_d^{\hat{r}}$ is fed back in a closed-loop fashion using zero as reference—hence, the alignment–and a PI regulator is used to generate the estimated rotor speed $\hat{\omega}_r$. The estimated rotor position $\hat{\theta}_r$ is consecutively obtained through the integration of $\hat{\omega}_r$.

Fig. 6 also shows the use state feedback linearization—by means of gain G_{lin}–thus ensuring a constant linear dynamic response of the tracking controller regardless of the PMSM rotor speed. This linearization gain is defined by

$$G_{\mathrm{lin}} = \frac{-1}{\sqrt{\hat{e}_d^2 + \hat{e}_q^2}}. \tag{17}$$

The resultant closed-loop response of the tracking controller after linearization is then the following one:

$$\frac{\hat{e}_d^{\hat{r}}(s)}{e_{d\_\mathrm{ref}}^{\hat{r}}(s)} = \frac{k_{pt}s + k_{it}}{s^2 + k_{pt}s + k_{it}}. \tag{18}$$

The gains of the tracking controller k_{pt} and k_{it} are then determined by setting the desired closed-loop response according to the following second-order polynomial:

$$s^2 + 2\zeta\omega_t s + \omega_t^2 \tag{19}$$

which yields the following proportional and integrative gains:

$$k_{pt} = 2\zeta\omega_t \qquad k_{it} = \omega_t^2. \tag{20}$$

Fig. 7(a) shows the actual and estimated rotor speed and rotor position depicting the PLL-based tracking controller response once the state observer is enabled at time $t = 0.1$ s. The figure shows the anticipated alignment achieved by the proposed strategy, showing a slight overshoot in correspondence with its damping coefficient selection. Fig. 7(b) similarly shows the actual and estimated rotor speed and rotor position obtained with the angular-error-based tracking controller using (16) [11]. Just as in the previous case, the state observer is enabled at time $t = 0.1$ s, where, now, a much faster response with an overshoot twice as high as for the PLL-based tracking controller is observed, clearly not in compliance with the design specifications.

The aforementioned dynamic response is verified in Fig. 8, which shows the frequency response obtained with the PLL-based tracking controller. Fig. 8(a) shows the controller loop gain with a crossover frequency of 60 Hz, in correspondence with the design specifications, and Fig. 8(b) shows the closed-loop response depicting its resonant peak at 60 Hz.

VII. Vector Control Strategy

A. Current Controller

Fig. 9 shows the structure of the $d{-}q$-axis current regulator used. Both channels employ a PI controller with additional

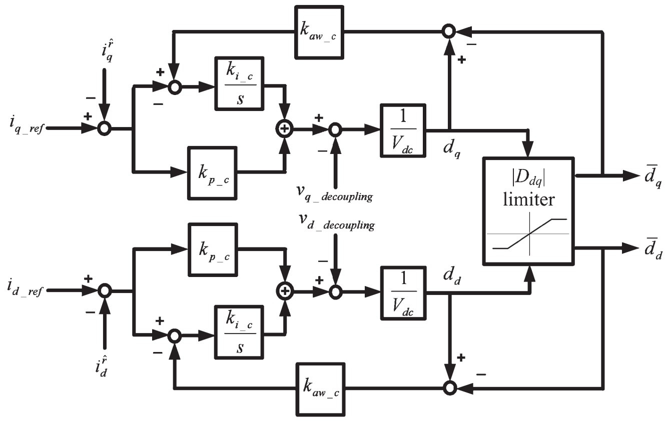

Fig. 9. PI controller implementation for $d-q$-axis current loop including antiwindup protection using a duty-cycle $d-q$ modulus limiter.

decoupling terms used to cancel out the dynamic interactions between them. These are defined as

$$v_{d\_\text{decoupling}} = -\hat{\omega}_r L_s i_{qs}^{\hat{r}} \quad (21)$$
$$v_{q\_\text{decoupling}} = \hat{\omega}_r L_s i_{ds}^{\hat{r}} + \hat{\omega}_r \lambda_m. \quad (22)$$

The resultant ac dynamics are then simply given by

$$v_{ds}^{\hat{r}} = R_s i_{ds}^{\hat{r}} + L_s \frac{d}{dt} i_{ds}^{\hat{r}} \quad (23)$$
$$v_{qs}^{\hat{r}} = R_s i_{qs}^{\hat{r}} + L_s \frac{d}{dt} i_{qs}^{\hat{r}}. \quad (24)$$

Then, if the PI gains k_{p_c} and k_{i_c} are made proportional to the desired closed-loop bandwidth ω_c

$$k_{p\_c} = L_s \omega_c \qquad k_{i\_c} = R_s \omega_c \quad (25)$$

the closed-loop transfer functions for both $d-q$-axis current loops may be derived using Fig. 9 and (23) and (24)—converted into the s-domain. These are given by

$$\frac{i_{ds}^{\hat{r}}(s)}{i_{ds\_\text{ref}}(s)} = \frac{i_{qs}^{\hat{r}}(s)}{i_{qs\_\text{ref}}(s)} = \frac{\omega_c}{s+\omega_c}. \quad (26)$$

The bandwidth of $d-q$-axis current regulator is defined as 50 times that of the speed control loop; hence,

$$\omega_c = 50 \cdot \omega_s. \quad (27)$$

The antiwindup scheme used is presented in [12], where the antiwindup gain is defined as

$$k_{\text{aw}\_c} = \frac{k_{i\_c}}{k_{p\_c}} \quad (28)$$

and both PI gains must comply with

$$k_{p\_c} \geq R_s \qquad k_{i\_c} \leq \frac{k_{p\_c}^2}{(1+\sqrt{2})\, L_s}. \quad (29)$$

B. Speed Controller

Fig. 10(a) shows a conventional closed-loop speed control scheme for PM machines. The open-loop and closed-loop transfer functions derived from Fig. 10 are given by

$$G_{s\_\text{ol}}(s) = \frac{k_{p\_s}s + k_{i\_s}}{s} \frac{K_T}{J_m s} \frac{P}{2} \quad (30)$$
$$G_{s\_\text{cl}}(s) = \frac{K_T P}{2} \frac{k_{p\_s}s + k_{i\_s}}{J_m s^2 + (k_{p\_s}s + k_{i\_s}) \frac{K_T P}{2}}. \quad (31)$$

The motor-drive mechanical dynamics are given by

$$J_m \frac{d}{dt}\omega_r + B_m \omega_r = \frac{P}{2}(T_e - T_L) \quad (32)$$

where all constants are defined in the Appendix.

In order to improve the transient performance of the speed loop, a filter precompensator is added to cancel out the zero introduced by the speed-loop PI as shown in Fig. 10(b). This prefilter is defined as

$$G_{s\_f}(s) = \frac{k_{i\_s}}{k_{p\_s}s + k_{i\_s}}. \quad (33)$$

The PI regulator and filter precompensator parameters are then defined as

$$k_{p\_s} = 2\zeta\omega_s \cdot \frac{2J_m}{K_T P} \qquad k_{i\_s} = \omega_s^2 \cdot \frac{2J_m}{K_T P}. \quad (34)$$

This results in the following second-order closed-loop dynamics for the motor-drive speed loop:

$$G_{s\_\text{cl}}(s) = \frac{\omega_r(s)}{\omega_{r\_\text{ref}}(s)} = \frac{\omega_s^2}{s^2 + 2\zeta\omega_s s + \omega_s^2}. \quad (35)$$

As shown in Fig. 10(b), this control loop also employs an antiwindup scheme, with its gain defined as

$$k_{\text{aw}\_s} = \frac{k_{i\_s}}{k_{p\_s}}. \quad (36)$$

In order to ensure operation within the linear range of the closed-loop system, the PI gains should be limited to the following values per [12]:

$$k_{p\_s} \geq B_m \qquad k_{i\_s} \leq \frac{k_{p\_s}^2}{(1+\sqrt{2})\, J_m}. \quad (37)$$

These restrictions provide a lower boundary for the speed-loop damping coefficient, which may be found by replacing (34) into (37) as shown in the following:

$$\zeta^2 \geq \frac{K_T P}{8}\left(1+\sqrt{2}\right). \quad (38)$$

C. Flux-Weakening Controller

Many different strategies have been developed for the flux-weakening control of PM machines; this paper presents an approach based on [13]. The operation beyond the machine base speed requires the PWM inverter to provide output voltages higher than its output capability—limited by its dc-link voltage–which in turn saturates the motor-drive control system if no precautions are taken. The absolute maximum duty cycle corresponding to the inverter voltage vector is defined as $\|D_{dq}\|$. By simple inspection of the machine model, it may

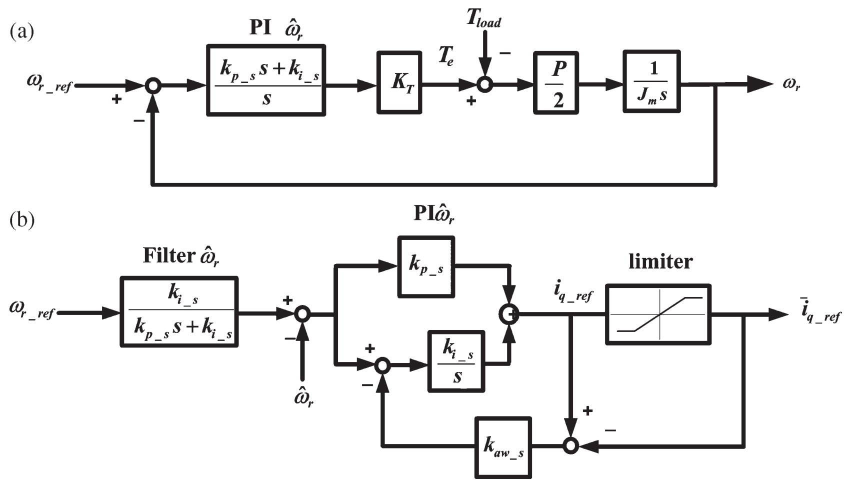

Fig. 10. Block diagram of speed-loop control system showing (a) speed loop and (b) PI with precompensator filter and antiwindup loop.

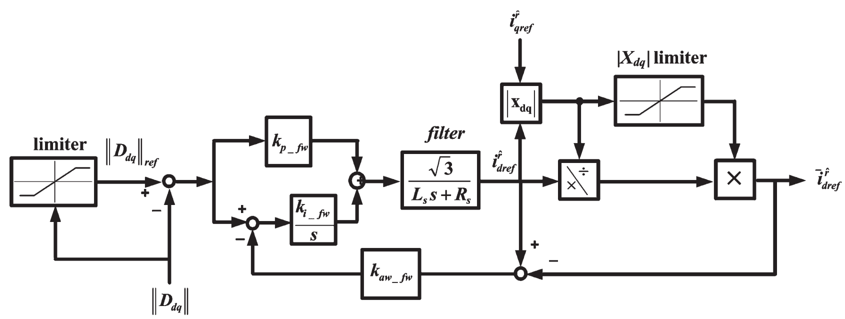

Fig. 11. Flux-weakening controller implementation with antiwindup action and D-axis current limiter based on q-axis current reference.

be found that injecting d-axis current into the machine has the desired effect of weakening its field and, hence, the need for higher voltages as the machine exceeds its base speed. An antisaturation control loop is then implemented in this paper to regulate the duty cycle to a desired maximum value under this condition, using, as control variable, the d-axis current (Fig. 11). Since the current-loop bandwidth is defined as 50 times faster than the speed loop, its closed-loop transfer function may be approximated to unity as shown in the following:

$$\frac{i^{\hat{r}}_{ds}(s)}{i_{ds\_\mathrm{ref}}(s)} = \frac{\omega_c}{s+\omega_c} \approx 1. \tag{39}$$

The d-axis current to duty-cycle transfer function, on the other hand, may be obtained from (23)—the linear machine model after decoupling and linearization—which simply yields the inverse of the machine dynamics as follows:

$$\frac{d^{\hat{r}}_d(s)}{i^{\hat{r}}_{ds}(s)} = \frac{1}{\sqrt{3}}\left(L_s s + R_s\right). \tag{40}$$

With (39) and (40) the comprising the flux-weakening plant model, the antisaturation controller may be defined as

$$PI_{\|Ddq\|}(s) = \frac{k_{p\_\mathrm{fw}}s + k_{i\_\mathrm{fw}}}{s} \cdot \frac{\sqrt{3}}{L_s s + R_s} \tag{41}$$

where the cascaded filter to the PI regulator cancels out the plant dynamics in (40). The resultant closed-loop transfer function has the following form:

$$\frac{\|D_{dq}\|(s)}{\|D_{dq}\|_{\mathrm{ref}}(s)} = \frac{k_{p\_\mathrm{fw}}s + k_{i\_\mathrm{fw}}}{(1+k_{p\_\mathrm{fw}})s + k_{i\_\mathrm{fw}}}. \tag{42}$$

The proportional and integrative gains of the PI regulator are defined by

$$k_{p\_\mathrm{fw}} = \omega_{\mathrm{fw}} \qquad k_{i\_\mathrm{fw}} = \omega^2_{\mathrm{fw}} \tag{43}$$

where ω_{fw} is the desired bandwidth defined as

$$\omega_{\mathrm{fw}} = 0.75 \cdot \omega_s. \tag{44}$$

Since this loop injects currents to avoid saturation of the motor-drive control system, the use of limiters becomes mandatory to protect the inverter and machine. In this case, the torque capability of the drive was given higher priority; hence, the d-axis current was limited to

$$i^{\hat{r}}_{\mathrm{dref}} \leq \sqrt{I^2_n - {i^{\hat{r}}_{\mathrm{qref}}}^2} \tag{45}$$

where I_n is the nominal current magnitude. Accordingly, the antiwindup scheme used the following gain:

$$k_{\mathrm{aw\_fw}} = \frac{k_{i\_\mathrm{fw}}}{k_{p\_\mathrm{fw}}} \tag{46}$$

with the proportional and integrative gains limited to

$$k_{p\_\mathrm{fw}} \geq 1 \qquad k_{i\_\mathrm{fw}} \leq \infty. \tag{47}$$

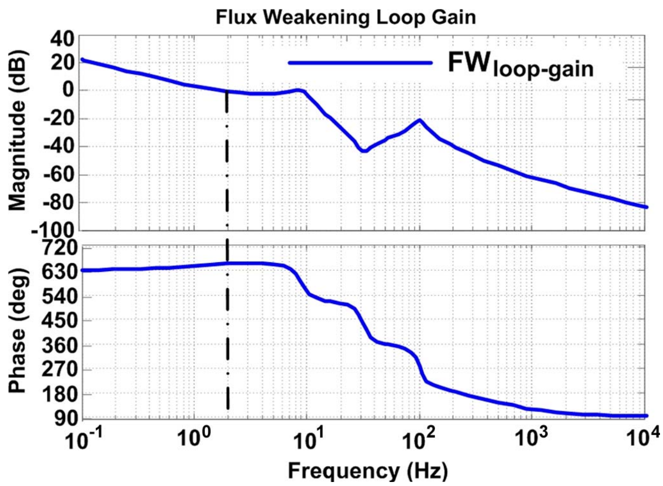

Fig. 12. Simulation result: Loop gain of the proposed antisaturation flux-weakening controller.

TABLE I
SENSORLESS VECTOR CONTROL BANDWIDTHS

Control Loop	Symbol	Value [p.u.]
Speed Controller	ω_s	1
Current Controller	ω_c	50
Flux weakening controller	ω_{fw}	0.75
Tracking controller	ω_t	20
State observer	ω_o	200

Fig. 12 shows the frequency response of the proposed antisaturation flux-weakening controller, depicting the loop-gain Bode plot and how the cutoff frequency of 2.25 Hz is effectively attained (given the 3-Hz speed-loop bandwidth).

VIII. EXPERIMENTAL RESULTS

Table I summarizes the design bandwidths for each of the control loops of the proposed strategy, which, for the previous design example ($\omega_s = 3$ Hz), defined the following bandwidths for the current controller, flux weakening, tracking controller, and state observer: 150, 2.25, 60, and 600 Hz.

The dynamometer setup used in this work is shown in Fig. 13. It comprises a four-quadrant 10-kW motor drive on the load side and a 7.5-kW motor drive on the test side. The two systems are coupled with an HBM MP60 torque and speed transducer. An N4L PSM 1600 frequency-response analyzer is used for generating the loop gain plots. The injection signal amplitude for loop gain plots was limited to 0.05 p.u. Experimental verification of the attained bandwidth for each control loop is presented in the time and frequency domains in the following subsections.

A. Back-EMF State Observer

Fig. 14(a) shows the startup sequence of the machine and corresponding operation of the state observer in speed closed loop. The reference speed ω_r^* was set at 0.15 p.u. that corresponds to an electrical frequency of 30 Hz. As explained in Section III, the initial and the threshold speeds were set at 0.05 and 0.08 p.u., respectively.

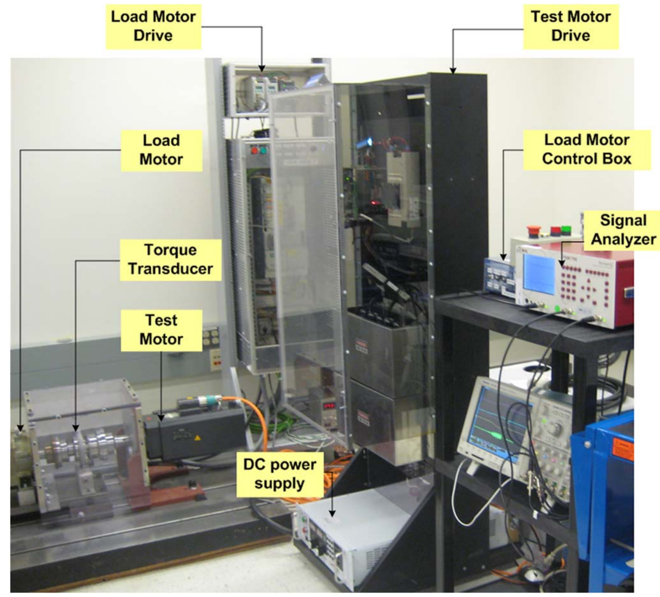

Fig. 13. Experimental setup for the validation of sensorless vector control.

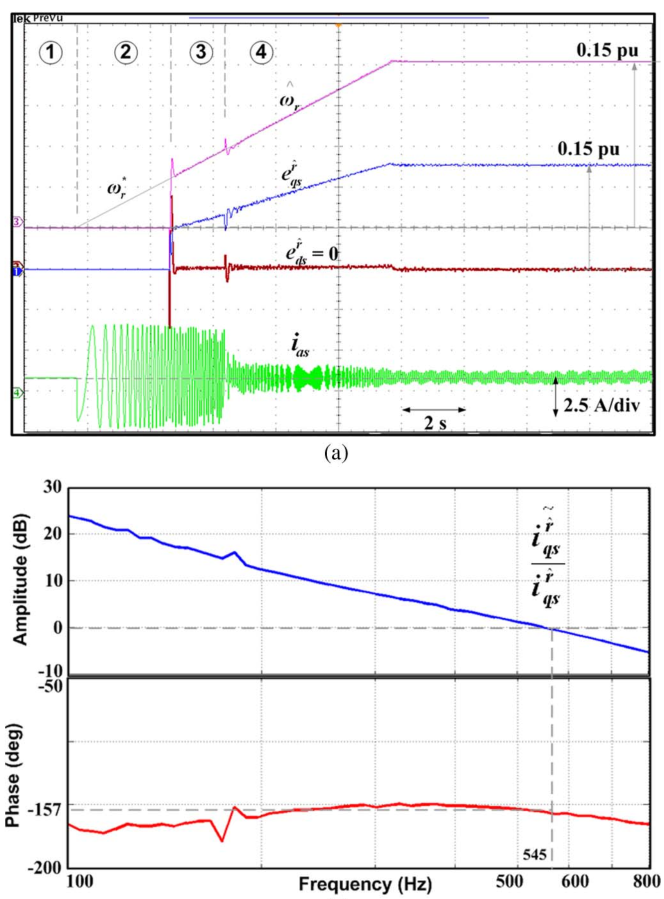

(a)

(b)

Fig. 14. Experimental results. (a) Machine startup operation under no load highlighting reference and estimated speed, q- and d-axis estimated back EMF, and phase current. (b) State observer open-loop gain highlighting the ratio of the estimated q-axis current error to the observer estimated current.

The observer is enabled in *Region 3* once the machine has left standstill and passed the prespecified initial speed. After being enabled, the estimated d- and q-axis back EMFs rapidly

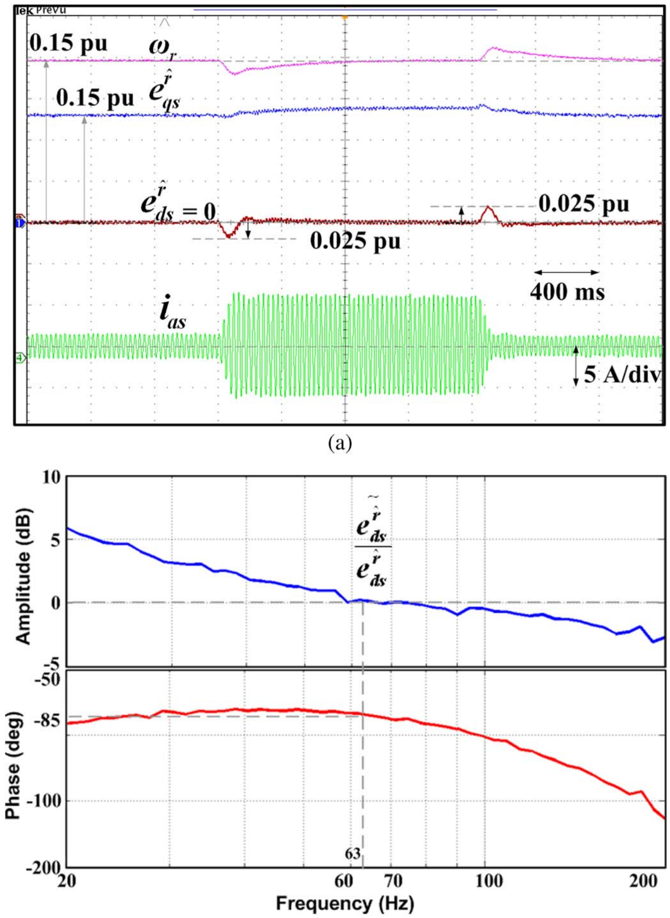

(a)

(b)

Fig. 15. Experimental results. (a) Operation with 50% step change in load torque highlighting estimated speed, q- and d-axis estimated back EMF, and phase current. (b) Tracking controller open-loop gain highlighting ratio of estimated d-axis back-EMF error to the estimated d-axis back EMF.

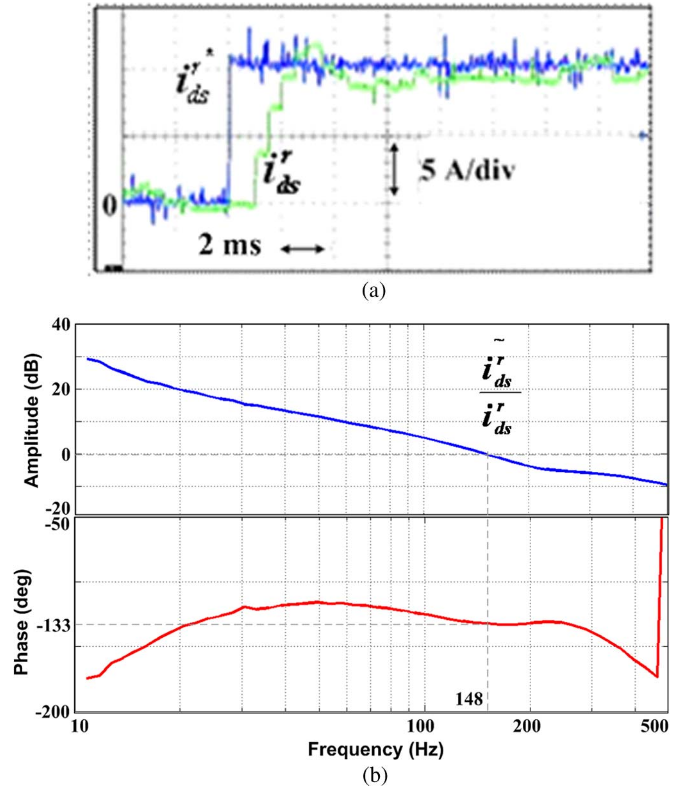

(a)

(b)

Fig. 16. Experimental results. (a) Stator d-axis current transient operation 0–10-A step change in reference and measured currents. (b) Current controller open-loop gain highlighting ratio of d-axis current error to the measured d-axis current.

converge to their estimated values as shown in Fig. 14(a). When the reference speed equals the predefined threshold speed, the speed loop is closed, and, at the same time, the reference currents are switched from their open-loop predefined values to the corresponding speed and antisaturation regulator outputs; hence, the sudden drop in the phase current at the onset of *Region 4* occurs. It should be noted that, in case of full position sensor feedback closed-loop vector control, the q- and d-axis back-EMF voltages follow the linear relation $e_{qs} = \omega_r \lambda_m$, while $e_{ds} = 0$. Although some deviation from the aforementioned condition is seen during acceleration in sensorless mode of operation, the relationship is satisfied during steady state and is seen in *Region 4*. Fig. 14(b) shows the state observer open-loop gain as the ratio of estimated q-axis current error to the observer estimated current. The gain crossover frequency is 545 Hz, and the corresponding phase margin at this frequency is 23°. The distortion in the frequency response at 180 Hz is due to the inverter dead time which induces a sixth-harmonic frequency component in the estimated d- and q-axis currents. This effect can be minimized by applying dead-time compensation algorithm. It should also be mentioned that the motor back EMF is devoid of higher ordered harmonics and is purely sinusoidal. Observers with a nonsinusoidal back EMF must be evaluated separately and is beyond the scope of this work.

As explained in Section V, in a two-stage approach, it is essential to have the appropriate time scale separation between the back-EMF observer and the tracking controller; accordingly, the combined performance along with speed controller will be discussed in the next subsection.

B. Tracking Controller

Once the state observer operation is verified, the tracking controller may be readily tuned since its inputs correspond to the state observer outputs, i.e., the estimated $d{-}q$-axis back EMFs.

Fig. 15(a) shows the transient response of the speed and tracking controller to a 50% step change in load torque. As seen in Fig. 15(a), the controller depicts stable operation with estimated d-axis back EMF regulated to zero and with an undershoot of 2.5% for the step load. It can be seen that the estimated speed has a dynamic response which is much slower than the estimated d-axis back-EMF voltage. It can be noted that the phase current follows the tracking observer dynamics because the output of the tracking controller is the estimated speed and position which is used for the sensorless vector control. Fig. 15(b) shows the tracking controller open-loop gain highlighting ratio of estimated d-axis back-EMF error to the estimated d-axis back EMF. The gain crossover frequency is 63 Hz. The corresponding phase margin at this frequency is 95°.

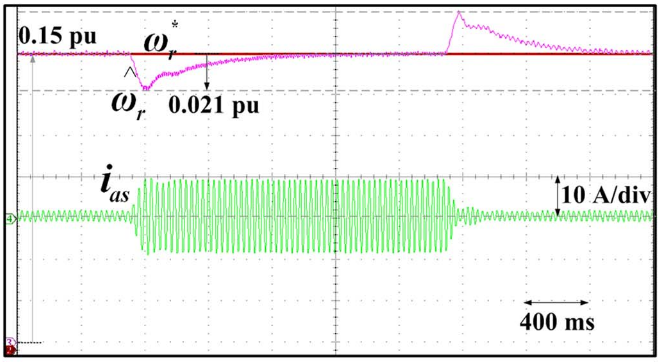

(a)

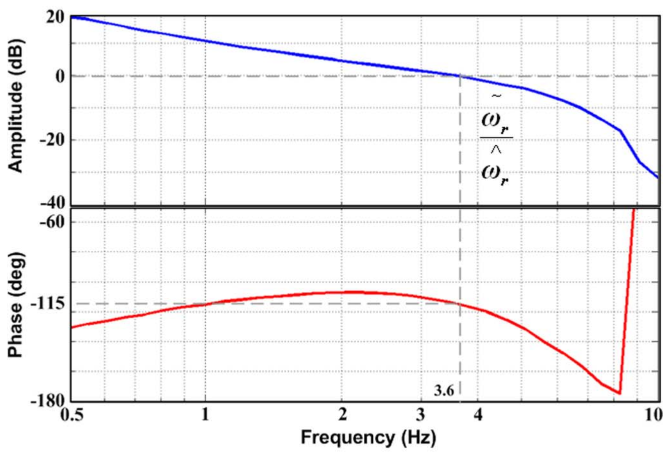

(b)

Fig. 17. Experimental results. (a) Machine transient operation with 75% step change in load torque highlighting estimated and reference speed and phase current. (b) Speed controller open-loop gain highlighting the ratio of speed error to the estimated speed.

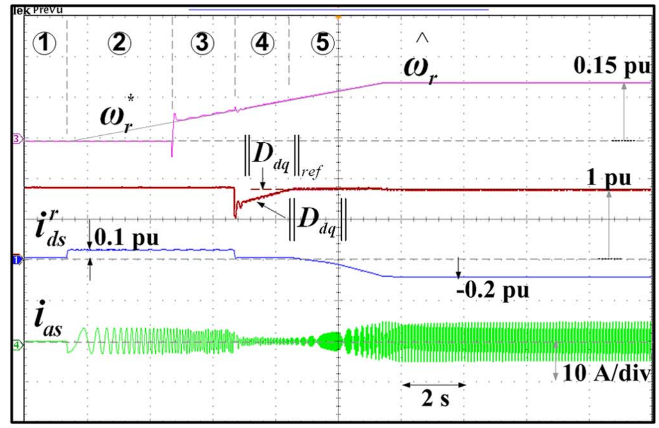

(a)

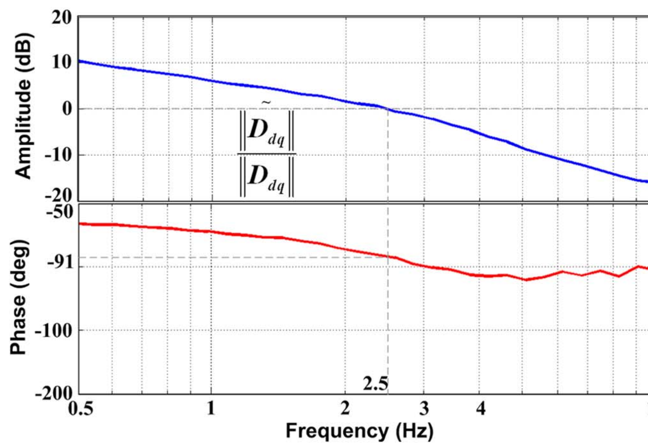

(b)

Fig. 18. Experimental results. (a) Machine startup including flux-weakening operation highlighting estimated and reference speed, reference and actual maximum duty cycle, measured d-axis current, and phase current. (b) Antisaturation flux-weakening controller open-loop gain highlighting ratio of error in magnitude of duty cycle to the actual duty cycle.

Once the state observer and tracking controller have been evaluated, the next subsection will elaborate on the performance of current regulator in estimated reference frame.

C. Current Controller

The current controller in estimated reference frame is evaluated by applying a step reference change on the d-axis. Fig. 16(a) shows the response of the motor drive, depicting a step change of 10-A peak. It can be seen that the current reaches steady state within 4 ms. The plot in Fig. 16(b) shows the current controller open-loop gain highlighting the ratio of d-axis current error to the measured d-axis current. The gain crossover frequency is 148 Hz, while the phase margin at this frequency is 47°. Since the machine does not have a salient rotor, the same bandwidths are applicable to both d- and q-axis current regulators. Considering the phase margin and the gain crossover frequency, the current controller open-loop bandwidth is within acceptable range in comparison to the design criteria. Then, it is essential to evaluate the speed controller response, and it will be discussed in the next subsection.

D. Speed Controller

The dynamic requirements for fan-type applications are low, and hence, low bandwidths are usually preferred. Fig. 17(a) shows a speed controller response to a 75% step load change from 0 to 15 $\mathrm{N \cdot m}$. A 14% undershoot is observed as the estimated speed returns to its reference value, while the phase current changes to 10 A. Although such load conditions are unlikely in the given application, the speed regulator performance demonstrated in Fig. 17(a) shows a stable operation by applying the controller explained in Section VII-B. Fig. 17(b) shows that the gain crossover frequency is 3.6 Hz, while the phase margin is 65°.

E. Antisaturation Flux-Weakening Controller

After verifying the anticipated operation of the current and speed loops, the antisaturation flux-weakening control loop was closed for its corresponding verification. The machine was operated at a dc-link voltage of 110 V in constant-torque region of operation and, then, at 100 V to allow the operation in the flux-weakening region. The reference speed was unchanged in both the operating modes.

Fig. 18(a) shows the machine startup operation including the flux-weakening region with focus on estimated speed, reference and actual maximum duty cycle, measured d-axis current, and phase current. The operation of the system is explained as follows. After rotor position is aligned in *Region 1*, the motor starts up in *Region 2* using current vector rotation with d-axis current defined at 0.1 p.u. Observer and tracking controllers are engaged in *Region 3* when the machine passes the prespecified initial speed. With the onset of Region 4, the speed loop is closed; correspondingly, the d-axis current is set to zero, while the q-axis current, which is the output of the speed regulator, generates the required torque to accelerate the motor. As the speed further increases, the maximum duty-cycle vector amplitude increases linearly, which is observed at the onset of *Region 4*. As the amplitude of this duty-cycle vector reaches 1 p.u., the inverter saturates to its voltage limit of 1 p.u.; however, the speed has yet to reach the reference value. It is then when the antisaturation regulator engages and generates a negative d-axis current to weaken the flux until the speed reaches its steady-state reference value of 0.15 p.u. It should be noted that the maximum duty-cycle vector is limited to its reference value of 1 p.u. The steady-state d-axis current amplitude achieved in this case is 0.2 p.u., which has resulted in an increase in the phase current amplitude.

Fig. 18(b) shows that the gain crossover frequency is 2.5 Hz while the phase margin is 89°. Overall, a stable operation is observed, including the transition from constant-torque *Region 4* to the flux-weakening *Region 5*, validating the controller structure defined in Section VII-C.

IX. Conclusion

This paper has presented a design methodology for the sensorless vector control of PMSM PWM motor drives in fan-type applications. Specifically, detailed derivations and design rules were given for all control loops—including antiwindup loops, verified through time-domain simulations; frequency-response analysis; and experimental results with a 7.5-kW PMSM motor drive. The proposed strategy used a two-stage approach based on a linear asymptotic state observer to estimate the machine back EMF and a novel PLL-based tracking controller used to estimate the machine speed and rotor position, achieving linear dynamics throughout the complete operating region. Vector controls were implemented over the estimation engine featuring the following: linear and decoupled dynamics, transient-performance optimized speed-loop controls, and inherent flux-weakening operation attained through an antisaturation control loop. The results presented throughout this paper validate the proposed design and control methodology.

Appendix

The following are the PMSM motor-drive parameters used:

Symbol	Value
r_s	0.37 Ω;
L_s	4.3 mH;
λ_m	0.1774 V_p/rad/s;
poles (P)	8;
speed	3000 r/min;
torque	20 N · m;
power	7.5 kW;
inertia J_m	$1.2m$ kg · m^2.

Acknowledgment

The authors would like to thank Dr. V. Blasko, from the United Technologies Research Center, for providing the laboratory facilities to carry out the experimental work.

References

[1] B. H. Bae, S. K. Sul, J. H. Kwon, and J. S. Byeon, "Implementation of sensorless vector control for super-high-speed PMSM for turbo-compressor," *IEEE Trans. Ind. Appl.*, vol. 39, no. 3, pp. 811–818, May/Jun. 2003.

[2] R. Wu and G. R. Slemon, "A permanent magnet motor drive without a shaft sensor," *IEEE Trans. Ind. Appl.*, vol. 27, no. 5, pp. 1005–1011, Sep./Oct. 1991.

[3] R. B. Sepe and J. H. Lang, "Real-time observer-based (adaptive) control of permanent-magnet synchronous motors without mechanical sensors," *IEEE Trans. Ind. Appl.*, vol. 28, no. 6, pp. 1345–1352, Nov./Dec. 1992.

[4] K. R. Shouse and D. G. Taylor, "Sensorless velocity control of permanent-magnet synchronous motors," *IEEE Trans. Control Syst. Technol.*, vol. 6, no. 3, pp. 313–324, May 1998.

[5] S. Bolognani, R. Oboe, and M. Zigliotto, "Sensorless full-digital PMSM drive with EKF estimation of speed and rotor position," *IEEE Trans. Ind. Electron.*, vol. 46, no. 1, pp. 184–191, Feb. 1999.

[6] J.-S. Kim and S.-K. Sul, "High performance PMSM drives without rotational position sensors using reduced order observer," in *Conf. Rec. IEEE IAS Annu. Meeting*, Oct. 1995, vol. 1, pp. 75–82.

[7] J.-S. Kim and S.-K. Sul, "New approach for high-performance PMSM drives without rotational position sensors," *IEEE Trans. Power Electron.*, vol. 12, no. 5, pp. 904–911, Sep. 1997.

[8] Y.-C. Son, B.-H. Bae, and S.-K. Sul, "Sensorless operation of permanent magnet motor using direct voltage sensing circuit," in *Conf. Rec. IEEE IAS Annu. Meeting*, Oct. 2002, vol. 3, pp. 1674–1678.

[9] T. Kailath, *Linear Systems*. Englewood Cliffs, NJ: Prentice-Hall, 1980.

[10] D. G. Luenberger, "An introduction to observers," *IEEE Trans. Autom. Control*, vol. AC-16, no. 6, pp. 596–602, Dec. 1971.

[11] R. D. Lorenz and K. W. Van Patten, "High-resolution velocity estimation for all-digital, AC servo drives," *IEEE Trans. Ind. Appl.*, vol. 27, no. 4, pp. 701–705, Jul./Aug. 1991.

[12] H.-B. Shin, "New antiwindup PI controller for variable-speed motor drives," *IEEE Trans. Ind.Electron.*, vol. 45, no. 3, pp. 445–450, Jun. 1998.

[13] J.-M. Kim and S.-K. Sul, "Speed control of interior permanent magnet motor for flux weakening operation," in *Conf. Rec. IEEE IAS Annu. Meeting*, Oct. 1995, vol. 1, pp. 216–221.

[14] K. Astrom and T. Hagglund, *PID Controllers: Theory, Design, and Tuning*. Research Triangle Park, NC: Instrum. Soc. Amer., 1995.

Parag Kshirsagar (S'01–M'07) received the B.E. degree in electrical engineering from the University of Pune, Pune, India, in 2000 and the M.S. degree in electrical engineering from Tennessee Technological University, Cookeville, in 2003. He is currently working toward the Ph.D. degree in electrical engineering at Virginia Polytechnic Institute and State University (Virginia Tech), Blacksburg, under the supervision of Prof. Krishnan Ramu.

In 2004, he was a Research Intern with Yaskawa Electric America, Waukegan, IL. From August 2004 to May 2007, he was a Research Assistant with the Center for Power Electronics Systems, Virginia Tech, where he worked on projects related to aerospace applications. In May 2007, he joined the United Technologies Research Center, East Hartford, CT, as a Senior Research Engineer in the power electronics group, where he has been a Staff Engineer and a Principal Investigator on projects related to electric motor-drive systems since 2011. He has three pending patents. His areas of interest include power converter topologies, pulsewidth modulation techniques, high-efficiency high-speed motor drives, sensorless control algorithms, magnetic bearing systems, and motor design.

Mr. Kshirsagar is an active member and Reviewer for the IEEE Industry Application Society and IEEE Transactions on Power Electronics. Since 2010, he has been serving as a Topic Chair and Session Chair at the Energy Conversion Congress and Exposition for the Electric Drives Committee.

Rolando P. Burgos (S'96–M'03) received the B.S. degree in electronics engineering, the Electronics Engineering Professional degree, and the M.S. and Ph.D. degrees in electrical engineering from the University of Concepción, Concepción, Chile, in 1995, 1997, 1999, and 2002, respectively.

In 2002, he joined, as a Postdoctoral Fellow, the Center for Power Electronics Systems, Virginia Polytechnic Institute and State University (Virginia Tech), Blacksburg, becoming a Research Scientist in 2003 and a Research Assistant Professor in 2005. In 2009, he joined, as a Scientist, ABB Corporate Research, USCRC, Raleigh, NC, where, since 2010, he has been the Principal Scientist. In 2010, he was also appointed Adjunct Associate Professor with the Department of Electrical and Computer Engineering, North Carolina State University, Raleigh. His research interests include multiphase multilevel power conversion, stability of ac and dc power electronics systems, hierarchical modeling, control theory and applications, and the synthesis of power electronics conversion systems.

Prof. Burgos is a member of the IEEE Power Electronics Society, where he currently serves as an Associate Editor for the IEEE POWER ELECTRONICS LETTERS and the IEEE TRANSACTIONS ON POWER ELECTRONICS.

Jihoon Jang (S'01–M'07) received the B.S., M.S., and Ph.D. degrees in electrical engineering from Seoul National University, Seoul, Korea, in 1999, 2001, and 2006, respectively.

He visited the Center for Power Electronics Systems, Virginia Polytechnic Institute and State University, Blacksburg, as a Visiting Scholar for one year, from September 2003 to September 2004, where he worked on the development of the permanent-magnet synchronous machine (PMSM) control systems for starter/generator and electric pump/fan applications. From January 2006 to September 2008, he was a Senior Research Engineer with the Hybrid System Engineering Team, R&D Center, Hyundai Motor Company, Hwaseong, Korea, where he developed the interior-type PMSM drive systems for the traction drives in the Elantra and Sonata hybrid electric vehicles. Since 2008, he has been with the General Motors Advanced Technology Center, Torrance, CA, where he is currently working on the electric machine drive systems for electric/hybrid electric/fuel cell electric vehicles. His current research interests include power electronic energy conversion systems, ac machine control systems including speed/position-sensorless control techniques, and fault-tolerant systems.

Dr. Jang serves regularly as a Reviewer for the papers submitted to the IEEE-sponsored international conferences including ECCE, ECCE Europe, ECCE Asia, Applied Power Electronics Conference, and Power Electronics and Drive Systems, and international journals published by IEEE in the area of power electronics and industry applications.

Alessandro Lidozzi received the B.S. degree in electronic engineering and the Ph.D. degree from Roma Tre University, Rome, Italy, in 2003 and 2007, respectively.

During 2005–2006, he was a Visiting Scholar with the Center for Power Electronics Systems, Virginia Polytechnic Institute and State University, Blacksburg. He is currently with Roma Tre University, where he was a Laboratory Technician from 2007 to 2010 and has been a Researcher with the Department of Mechanical and Industrial Engineering since 2010. His research interests are mainly focused in multiconverter-based applications, dc–dc power converter modeling and control, control of permanent-magnet motor drives, and control aspects for power electronics in diesel–electric units.

Dr. Lidozzi was a recipient of a Student Award and a Travel Grant at the International Symposium on Industrial Electronics in 2004.

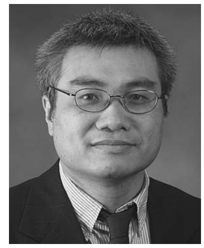

Fei Wang (S'85–M'91–SM'99–F'10) received the B.S. degree in electrical engineering from Xi'an Jiaotong University, Xi'an, China, in 1982 and the M.S. and Ph.D. degrees in electrical engineering from the University of Southern California, Los Angeles, in 1985 and 1990, respectively.

From 1990 to 1992, he was a Research Scientist with the Electric Power Laboratory, University of Southern California. In 1992, he joined the GE Power Systems Engineering Department, Schenectady, NY, as an Application Engineer. From 1994 to 2000, he was a Senior Product Development Engineer with GE Industrial Systems, Salem, VA. During 2000–2001, he was the Manager of the Electronic and Photonic Systems Technology Laboratory, GE Global Research Center, Schenectady, and Shanghai, China. In 2001, he joined the Center for Power Electronics Systems (CPES), Virginia Polytechnic Institute and State University, Blacksburg, as a Research Associate Professor, where he became an Associate Professor in 2004 and served as the CPES Technical Director beginning in 2003. Since 2009, he has been with The University of Tennessee, Knoxville, and Oak Ridge National Laboratory, Oak Ridge, TN, as a Professor and Condra Chair of Excellence in Power Electronics. He is a founding member and Technical Director of the multiuniversity National Science Foundation/Department of Energy Engineering Research Center for Ultra-wide-area Resilient Electric Energy Transmission Networks led by The University of Tennessee. His research interests include power electronics, power systems, controls, electric machines, and motor drives.

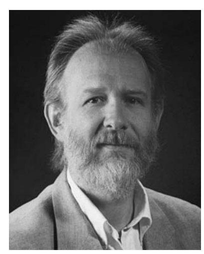

Dushan Boroyevich (S'81–M'86–SM'03–F'06) received the Dipl.Ing. degree from the University of Belgrade, Belgrade, Serbia, in 1976, the M.S. degree from the University of Novi Sad, Novi Sad, Serbia, in 1982, and the Ph.D. degree from Virginia Polytechnic Institute and State University (Virginia Tech), Blacksburg, in 1986.

From 1986 to 1990, he was an Assistant Professor and Director of the Power and Industrial Electronics Research Program with the Institute for Power and Electronic Engineering, University of Novi Sad, where he later became the Acting Head. He then joined Virginia Tech as an Associate Professor, where he is currently the American Electric Power Professor with the the Bradley Department of Electrical and Computer Engineering and Codirector of the Center for Power Electronics Systems. His research interests include multiphase power conversion, electronic power distribution systems, power electronics system modeling and control, and multidisciplinary design optimization.

Dr. Boroyevich is a recipient of the IEEE William E. Newell Power Electronics Technical Field Award. He is the 2011–2012 President of the IEEE Power Electronics Society.

Seung-Ki Sul (S'78–M'87–SM'98–F'00) was born in Korea in 1958. He received the B.S., M.S., and Ph.D. degrees in electrical engineering from Seoul National University, Seoul, Korea, in 1980, 1983, and 1986, respectively.

From 1986 to 1988, he was an Associate Researcher with the Department of Electrical and Computer Engineering, University of Wisconsin, Madison. From 1988 to 1990, he was a Principal Research Engineer with Goldstar Industrial Systems Company. He is currently with Seoul National University, where he has been a member of the faculty of the School of Electrical Engineering since 1991, was Vice Dean of the College of Engineering from 2005 to 2007, and is currently a Full Professor. From 2003 to 2004, he was a Research Director and Acting Consultant with Yaskawa Electric Corporation, Japan. He has published over 120 reviewed journal papers, mainly in IEEE TRANSACTIONS. He is the holder of 13 U.S. patents and granted 36 Ph.D. degrees under his supervision.

Dr. Sul was the President of the Electrical Engineering Science Research Institute funded by the Korean Government from 2008 to 2011. He was the Technical Chair of the IEEE Power Electronics Specialist Conference 2006 and General Chair of IEEE ECCE Asia 2011.